

Nuclear Morphology Optimized Deep Hybrid Learning (NUMODRIL) For Accurate Diagnosis and Prognosis of Ovarian Cancer

Duhita Sengupta

Saha Institute of Nuclear Physics

Sk Nishan Ali

Must Research, Telangana

Aditya Bhattacharya

Must Research, Telangana

Joy Mustafi

Must Research, Telangana

Asima Mukhopadhyay

Queen Elizabeth Hospital, Gateshead

KAUSHIK SENGUPTA (✉ kaushik.sengupta@saha.ac.in)

Saha Institute of Nuclear Physics

Research Article

Keywords: lamins, ovarian cancer, tissue microarray, confocal imaging, nuclear morphology, deep learning, deep hybrid learning

Posted Date: January 20th, 2021

DOI: <https://doi.org/10.21203/rs.3.rs-148149/v1>

License: © ⓘ This work is licensed under a Creative Commons Attribution 4.0 International License.

[Read Full License](#)

Abstract

Nuclear morphological features are potent determining factors for clinical diagnostic approaches adopted by pathologists to analyse the malignant potential of cancer cells. Considering the structural alteration of nucleus in cancer cells, various groups have developed machine learning techniques based on variation in nuclear morphometric information like nuclear shape, size, nucleus-cytoplasm ratio and various non-parametric methods like deep learning have also been tested for analysing immunohistochemistry images of tissue samples for diagnosing various cancers. Our aim is to study the morphometric distribution of nuclear lamin proteins as a specific parameter in ovarian cancer tissues. Besides being the principal mechanical component of the nucleus, lamins also present a platform for binding of proteins and chromatin thereby serving a wide range of nuclear functions like maintenance of genome stability, chromatin regulation. Altered expression of lamins in different subtypes of cancer is now evident from data across the world. It has already been elucidated that in ovarian cancer, extent of alteration in nuclear shape and morphology can determine degree of genetic changes and thus can be utilized to predict the outcome of low to high form of serous carcinoma. In this work, we have performed exhaustive imaging of ovarian cancer versus normal tissue and introduced a novel Deep Hybrid Learning approach on the basis of the distribution of lamin proteins. Although developed with ovarian cancer datasets in view, this architecture would be of immense importance in accurate and fast diagnosis and prognosis of all types of cancer associated with lamin induced morphological changes and would perform across small/medium to large datasets with equal efficiency.

Highlights

- We have performed an exhaustive morphological analysis of nuclei from tissues of ovarian cancer and normal ovary based on lamin A and lamin B staining pattern.
- Based on that we have developed a novel Deep Learning approach to classify normal and ovarian cancer tissues with highest accuracy and speed.
- This method is a tailored state-of-the-art deep hybrid network between classical machine learning algorithms (XGBoost, SVM, Random Forest) and standard CNN.
- Considering the probable potential of the pattern of nuclear lamin distribution in tissues to clinically validate malignancy and the novelty of the algorithm to distinguish ovarian cancer nuclei from normal nuclei, we propose that this may be used to predict malignant transformations of benign nuclei and can be implemented in early detection of ovarian cancer in future.
- In generalized terms this method can be extended as a valuable tool in the diagnosis and prognosis of any type of cancer which is associated with morphologically altered nuclei.

Introduction

The nuclear envelop is a double membrane structure encapsulating the lamina which is a thick meshwork of A & B-type lamin proteins. Nuclear lamins are type V intermediate filament proteins which impart

proper size and shape to the nucleus thus conferring mechanical stability¹. Lamins also provide a scaffold for binding of several proteins and chromatin. Lamins are associated with a wide range of nuclear functions like nuclear stability², genome organisation³, protein interaction⁴, DNA damage repair⁵, intracellular signalling⁶ and it has got vital roles in replication⁷, transcription⁸, and splicing⁹ as well. The mammalian genome encodes three genes for lamin proteins namely, LMNA, LMNB1 and LMNB2. LMNA is alternatively spliced into two major isoforms lamin A and lamin C and two minor isoforms, lamin C2 and AΔ10. LMNB1 codes for lamin B1 and LMNB2 codes for lamin B2 and lamin B3, the expression of human lamin B3 is restricted to the male germ line¹⁰. All these three types of lamin A, B and C form discrete self-interacting, independent meshwork but interconnected lattice structures with different physical properties¹¹. In mammals, B type lamins are ubiquitously expressed in all tissue types but lamin A and C are developmentally regulated and expressed in differentiated cells¹². Lamin A is not detectable in the embryonic stage but its expression sets in when the cells begin to proliferate and divide¹². Studies in monoblastoid cells have shown that induction of differentiation is associated with enhanced expression of lamin A/C along with lateral observations like reduced cell proliferation and stronger substratum contact. However, upon withdrawal of the inducer, proliferation kinetics was restored indicating retro-differentiation which was then accompanied by decreased levels of lamin A/C¹³. These studies lead to the hypothesis that lamin A/C might stabilize differentiation and thus its absence was a major driving force for rapid division in various tumor cells¹⁴. But in many tumor types, lamin A/C levels are found to be increased which in turn is associated with their aggressive metastatic potential, which cannot be explained by retro-differentiation¹⁵. Rather in these cases increased level of lamin A/C might play vital roles in tumour progression by helping the cells overcome the mechanical stress and resist DNA damage induced cell cycle arrest as it may also help in recruitment of DNA damage repair proteins. In either case, change in expression levels of lamin A/C largely remains a reliable prognostic marker for different tumor types and stages¹⁶. There has been a report which attributes molecular crowding events to higher degree of genetic rearrangements leading to nuclear enlargement¹⁷. Being the major architectural protein of animal cell nuclei, lamins must be playing a vital role in this alteration of size¹⁸. Loss of lamin or their mutations leading to deformed nuclear morphology has been widely studied by different groups¹. Interestingly, the differential expression pattern of lamins in different cancers has also been documented from research across the world¹⁹. Recent findings have demonstrated methods to study nuclear morphologies in the light of fluorescent imaging and deep learning²⁰.

Application of convolutional neural network pipelines in cancer diagnosis and detection has already been widely recognised and reported by different groups utilising different technical and biological parameters. Currently, rise in life expectancy is a global concern which is widely being triggered by increase in incidences in age related gynaecological cancers²¹. Morphometric studies in context of cancer has been thus far evaluated in only a few other carcinomas but not in a great detail in ovarian cancer. Detection of cancer from histopathology images and immunocytochemical staining is widely being studied worldwide²². On the other hand, alterations in nuclear morphology have been acclaimed as hallmarks in various cancers and are used majorly in pathology or diagnosis purposes by clinicians to verify the

degree of malignancy²³. But these verifications based on manual observations are never trustworthy. To circumvent this problem, researches have focussed on fluorescence imaging combined with machine learning for detection of malignancy. Various parametric and non-parametric methods are already in use for diagnosis of various cancers²⁴. Several groups have reported deep learning techniques to classify different stages or subtypes of ovarian cancer based on different techniques and biological features²⁵. These rely on different classifiers based on differential features due to shift from the familiar genomic or proteomic sketch of the non-cancerous counterpart. There are several methods to study alterations in various nuclear matrix proteins which are already reported to be used for cancer diagnosis like BLCA4 (Bladder and urothelial carcinoma protein 4) in bladder cancer²⁶, AR-V7 (Androgen Receptor splice variant 7) in prostate cancer²⁷ and NMP 179 (Nuclear Matrix Protein 179) in cervical cancer²⁸. But these data were essentially non-parametric or in other words, not based on specific annotations of prognostic markers.

In this work, our aim is to study the morphometric distribution of nuclear lamins in ovarian cancer tissues from patients. Being a resident of the nuclear periphery, lamin A and B, when visualized and imaged under confocal microscope in different ovarian cancer tissue samples, can give us information about the shape and size of the nucleus. In the present study on ovarian cancer model, we have introduced lamin A and B as specific markers for classification and accordingly designed an advanced deep hybrid learning (DHL) architecture which helped us extract information from the tissue types and classify them accordingly by deep hybrid learning algorithm which in turn can aid in pathological inspections proposing the ratio of lamin A and B to be clinically significant for diagnosing ovarian cancer. Consequently, this could be implemented to predict the onset and progression of ovarian cancer respectively. Systematic analyses of patient tissue samples in the form of tissue microarray (TMA) were accomplished by confocal imaging. This dataset of images were used as input for developing a fast and accurate deep hybrid learning method.

Materials And Methods

Tissue sample collection:

Formalin fixed paraffin embedded tissues from ovarian cancer patients (n=40) were obtained during frontline surgery at Tata Medical Center (TMC), Kolkata. Ethical approval for the study was obtained from Tata Medical Center Ethics committee (EC/TMC/45/15). Informed consent was obtained from all participants. An ovarian tissue micro array was created at TMC representing various stages of high grade serous ovarian cancer consisting of both Primary debulking surgery and interval debulking surgery tissues. Slides were provided without identifying any clinical data for unbiased analysis. All methods were carried out in accordance with relevant guidelines and regulations.

Immunohistochemistry:

The paraffin embedded blocks were cut into 4-5 μm sections and affixed onto glass slides. For removal of paraffin, the slides were immersed in xylene (3*10mins) followed by immersion in graded ethanol twice for 10 minutes in each (100%,95%,80%,70%), washed in ddH₂O twice for 5 minutes each. The tissues were immersed in 10mM sodium citrate buffer (pH 6), placed in a microwavable container, and heated at full power for 3 minutes and 80% power for subsequent 12 minutes. After which the slide was allowed to cool gradually in the same buffer, followed by rinsing with ddH₂O twice for 5 minutes each followed by two rounds of wash in PBS for 5 minutes each. Tissues were permeabilised with 0.5% Triton X 100 for 5 minutes, blocked and incubated with primary antibody solution containing blocking agent (5% Normal Goat Serum and Primary antibody as per dilution recommended in 1X PBS) in a humidified environment for 2 hours in room temperature. Subsequently cells were incubated with secondary antibody diluted in 1X PBS for 2 hours at dark in room temperature. Cells were finally incubated in Propidium Iodide at a concentration of 10 $\mu\text{g}/\text{ml}$ for 40 minutes and then mounted on glass slides with mounting medium containing anti oxidizing agent (PPD). It was sealed with nail polish and imaged using 63X oil immersion objectives in Zeiss LSM 710 Meta confocal Microscope. The slides were stored in dark at 4°C for further use. Primary antibody dilutions for Rabbit Anti Lamin A antibody (Sigma Aldrich L1293), Anti Lamin B (Santacruz sc-6217) antibody were 1:100 and 1:50 respectively. Secondary antibodies were conjugated with Alexa Fluor 488 (Green Fluorescence) and used at a dilution of 1:400. For Anti Lamin B antibody, methanol fixation was performed. Cells were fixed with ice cold methanol for 20 minutes at -20°C and permeabilised in Acetone for 1 minute in room temperature.

Image Analysis and data presentation:

Images were analysed using ImageJ software (ImageJ bundled with 64-bit Java 1.8.0_112). Considering each nucleus an ellipse, the equations used in the referred article²⁹ were followed to derive the values of the morphometric parameters like area, perimeter, loop length, circularity, eccentricity, foci distance, maximum curvature, normalized maximum curvature. Histograms were generated using ROOT data analysis framework (An object oriented C++ framework for large data storage, presentation, visualisation and statistical analysis) (Version 6, Release 6.08/06-2017-03-02). Each field from every tissue sample contained around 100 nuclei approximately. The length of the major and minor axes of each of the nuclei was measured manually by ImageJ. In the plots the X axis denotes the normalized number of nuclei with respect to the total number of nuclei calculated corresponding to the defined parameter and Y axis denotes the measure of the parameter. Mean, Standard error of mean and Standard deviation for the analysis of each parameter have been mentioned in the figure legends.

Pre-processing:

Although Deep Learning algorithms are believed to apply auto feature extraction methods, we wanted to additionally transform the raw data and make it easier for the model to unravel key features. Using morphological elliptical image filters, morphological masks were formed around the nuclei and then using Gaussian Blur filter and pixel weights addition, the sharpened version of the images were obtained. Then the images were grey-scaled and normalized before feeding it into the deep learning model.

Synthetic Minority Oversampling Technique (SMOTE):

Synthetic Minority Oversampling Technique (SMOTE)³⁰, uses vector interpolation techniques with high dimensional data to generate synthetic samples of the minority class. The synthetically generated samples are linear combinations of two similar samples from the minority class (x and x^R) and are defined as:

$$s = x + \mu \cdot (x^R - x)$$

where, x is a minority class sample and x^R is another minority class sample which is randomly picked from a sample space which has high similarity with x and is identified by nearest neighbour approach. The factor μ is randomly selected from a uniform distribution between 0 and 1 and it is the same for all dimensional variables, but it is different for different values of x . SMOTE keeps the same expected value of the synthetically generated minority class, but it decreases its variability, thereby making the SMOTE-augmented data statistically different and thus, does not add any bias to the data.

Deep Hybrid Learning Model Architecture:

The entire Deep Hybrid Learning architecture used for this research work starts with the pre-processing layer, then the pre-processed images are passed through the model input layer. Each input is of dimension (1024, 1024,4). Deep Hybrid Learner uses a Deep Convolutional Neural Network Layer for feature extraction. In our research we have used a 21 Layered CNN which is inspired from InceptionNet v3 architecture. The CNN part consisting of a series of Incept layers and Squeeze Layers which are like grouped Convolution Layers with specific hyper-parameters and the nested Conv2D layer is illustrated in Figure 1.

For the Incept Layer, it takes the number of filters for the Conv2D sub-layer and another hyper-parameter for the number of filters for Left and Right Conv2D sub-layer as input. In both the Conv2D sub-layers, after tuning, we have used a learning rate of 0.1 and an activation function of Leaky ReLu to learn the non-linear relationships in the underlying high dimensional data. For the initial Conv2D layer, we have used a filter dimension of 5x5 and used strided convolution with stride as 2. For Left Conv2D a filter size of 3x3 is used and for the Right Conv2D a filter size of 5x5 is used. Finally, both the left and right conv2d sub layers are concatenated and passed to the next layer. The Squeeze layer follows the same structure as Incept Layer. The learning rates and the activation function used in the sub-layers is the same, but the only difference is with the filter dimensions. For the initial Conv2D sub layer, the dimension is (1x1) and stride 1. While for Left Conv2D the filter dimension is (1x1) and for Right Conv2D the filter dimension is (3x3). Like the Incept layer, the Left and the Right Sub-layers are concatenated and passed to the next layers. After a series of Incept and Squeeze layers we have used another Conv2D layer with 64 filters and each filter is of dimension 3x3, with an activation function of Leaky ReLu with learning rate 0.1. Finally, after all the convolution layers which are used to extract the features, we have flattened the output and passed the flattened output to classical Machine Learning algorithms like XGBoost and Random Forest

for the final classification part. The overall scheme of deep hybrid learning used here is depicted in Figure 1.

Comparison of DHL with other Deep Learning approaches:

In order to evaluate how well our Deep Hybrid Learning (DHL) approach is performing on the training, validation and test dataset as compared to other popular Deep Learning approaches, we have used AUC Scores, Accuracy and Confusion Matrix as the evaluating metrics. In this research work we have compared the Deep Hybrid Learning with both XGBoost and Random Forest variant, with a conventional Deep Neural Network (without transfer learning and having the same 21 layered CNN as DHL), DenseNet201³¹ with transfer learning, InceptionNet v3 with transfer learning, ResNet50 with transfer learning and VGG16³² with transfer learning.

Results And Discussion

Distinct nuclear morphology of ovarian cancer tissues:

Formalin fixed paraffin embedded normal and diseased (ovarian cancer) tissues were obtained from Tata Medical Center following the ethical guidelines. Tissues were stained with lamin A, and lamin B following proper antigen retrieval technique and imaged under confocal microscope. Each field containing approximately 110-150 nuclei were captured from each of the subsets (lamin A stained Normal and Ovarian Cancer tissues, lamin B stained Normal and Ovarian Cancer tissues) under similar acquisition parameters. One representative field from each of the tissue sets has been shown in Figure 2. A visibly prominent enlargement of the cancer nuclei was observed with respect to the normal nuclei in both lamin A and lamin B stained tissues. Two tissue microarrays each containing 40 samples were obtained from Tata Medical Center for which we were blinded. The arrays were stained for lamin A and lamin B following the same procedure and consequently the images acquired from the TMA slides were used for validation of the best working model for this problem. 40 samples in a tissue microarray slide stained with lamin A antibody has been shown in Figure 3.

Data Augmentation by SMOTE and Analysis of data points in the sample space:

We started our experiment with 262 fields each containing about 150 nuclei of ovarian cancer tissues (majority class) and 52 fields each containing about 110 nuclei of normal ovarian epithelial tissue (minority class). Considering the dataset used, the distribution between the majority and the minority class was not equal and the majority class comprised of almost 84% of the dataset, and hence the dataset used was an imbalanced one. Using an imbalanced dataset for building a Deep Learning classifier would add bias to the majority class and unless the dataset is synthetically matched, the classifier would have a strong tendency to predict the majority class for unknown samples. Therefore, we have applied Synthetic Minority Oversampling Technique (SMOTE)³⁰, which uses vector interpolation with high dimensional data to generate synthetic samples of the minority class. Different properties of SMOTE have various implications over high dimensional data³³.

Image Pre-processing:

The pre-processing algorithm consists of two parts – applying a segmentation mask based on the key visual properties like area, perimeter, circularity, eccentricity, foci distance, loop length, maximum curvature and normalised curvature of the nuclei followed by image sharpening techniques. In the first part, based on the Image Hue Saturation Value (HSV) and using a sensitivity factor, the segmentation mask was created, which was subsequently made prominent by the application of morphological closing operation with an elliptical kernel. Elliptical kernel was used to adapt to the shape of the cells and capture the maximum possible relevant information. Rectangular kernel was previously tested and it got no more than 93% accuracy. In the second phase, using Gaussian Blur and adding weights to the blurred image, we ensured uniform sharpening of the pre-processed images with the segmentation masks and converted the pre-processed images into grey-scaled form so that the key visual features are made more prominent and easier for the Deep Learning algorithm to unravel features. Information from the background was completely removed to emphasize over the morphological properties of the nuclei. (Figure 4)

Morphometric comparisons between images before and after pre-processing:

The minor and major axes of each nucleus were measured manually using ImageJ (ImageJ bundled with 64-bit Java 1.8.0_112). Careful investigation revealed that the hallmark of the diseased tissues was characterized by prominent nuclear enlargement as reported earlier³⁴. We quantified these changes by considering every nucleus an ellipse; eight parameters (Area, Perimeter, Eccentricity, Circularity, Foci Distance, Loop Length, Maximum Curvature and Normalized Maximum Curvature) were measured for each of the nuclei using the formulae mentioned earlier²⁹. With these sets of images, a gross morphometric analysis was performed based on the distribution of lamin A and lamin B proteins in the nucleus. Later on, following pre-processing, all the eight parameters were reanalysed from the lamin A and lamin B stained nuclei on randomly selected cancer and normal pre-processed tissue images. Histograms were generated for each of the parameters using ROOT data analysis framework (Version 6, Release 6.08/06-2017-03-02), where the X axis denotes the normalized number of nuclei with respect to the total number of nuclei calculated corresponding to the defined parameter and Y axis denotes the measure of the parameter. It was evident from the plots (Figure 5), that the perimeter of most of the cancer nuclei from the total population were showing an increase of 55-62% compared to most of the normal nuclei for both lamin A and lamin B stained tissues in the images before pre-processing and the observation was similar in the pre-processed counterparts as well (Figure 5 A1, A2,A3, A4). Similar phenomena was observed while measuring the area, where the area of most of the cancer nuclei was more than twice the area of most of the normal nuclei in the population in both raw and pre-processed images of cancer and normal tissue (Figure 5 B1, B2,B3, B4). Both the observations indicated an increase in size of the cancerous nuclei and this feature was unaltered post pre-processing. However, in the cancer nuclei, around 3% and 12% shift from the normal were observed in the circularity and eccentricity values respectively which was not that significant denoting no prominent change in the shape (Supplementary figure 1 A1,A2,A3,A4, B1, B2,B3,B4). Eccentricity is a focal length (Distance from the centre to one focus) and semi major axis dependent variable. Still, to further validate, foci distance ($2 \times \text{Focal length}$) was also

measured where the shift associated with eccentricity was supposed to get doubled according to the formulae. We could find a small increase in the Foci distance values of the cancer nuclei in comparison to the normal nuclei, which denotes an increase in the distance between the foci thereby approaching an elliptical nature (Supplementary figure 1 C1, C2,C3,C4). Another common parameter in ellipse geometry is loop length, which is a focal length dependent variable, hence a rise was evident in the loop length of cancer nuclei denoting an increase in size once again (Supplementary figure 1 D1,D2,D3,D4). Next, to study the change in the surface architecture, maximum curvature and normalised curvature were measured; but no significant shift was observed to deduce a conclusion (Supplementary figure 1 E1, E2,E3,E4 F1, F2,F3,F4). Observations were consistent in the pre-processed images as well. As we all know, that tumor microenvironment harbours a heterogeneous cell population including cells at different stages of malignancy and some normal cells too, so the analysis spanned a large range of parametric measures to accommodate all the nuclei in the population. Some shifts were visibly clear and prominent but some were not. So, the change may not be specified with distinct values. Overall, these measurements confirmed prominent alteration in morphology in the cancer nuclei or in the nuclei approaching malignancy with respect to the normal nuclei and gave a gross idea regarding the direction of change. This experiment concluded that morphometric alteration in form of altered distribution of lamins in nuclei can potentially be used as signatures to classify cancer and normal nuclei or to study the progress towards malignancy and this feature being unaltered post pre-processing, can probably be a potential classifier for the deep learning model to distinguish between cancer and normal nuclei.

- A. 1. Comparative distribution of the number of normal (Mean±Std error of mean:17.82± 0.3032) (Std Dev:5.574±0.2144) and ovarian cancer (Mean±Std error of mean:27.59± 0.333) (Std Dev:6.626±0.2354) nuclei based on Perimeter values acquired from lamin A stained tissue images before pre-processing.
- A. 2. Comparative distribution of the number of normal (Mean±Std error of mean:16.11± 0.1259) (Std Dev:3.352±0.08) and ovarian cancer (Mean±Std error of mean:26.21± 0.3628) (Std Dev:7.814±0.2565) nuclei based on Perimeter values acquired from lamin B stained tissue images before pre-processing.
- A. 3. Comparative distribution of the number of normal (Mean±Std error of mean:13.75± 0.1804) (Std Dev:3.125±0.1276) and ovarian cancer (Mean±Std error of mean:23.1± 0.289) (Std Dev:5.445±0.2043) nuclei based on Perimeter values acquired from lamin A stained tissue images after pre-processing.
- A. 4. Comparative distribution of the number of normal (Mean±Std error of mean:12.85± 0.1732) (Std Dev:3.015±0.1225) and ovarian cancer (Mean±Std error of mean:23.66± 0.3121) (Std Dev:5.635±0.2207) nuclei based on Perimeter values acquired from lamin B stained tissue images after pre-processing.
- B. 1. Comparative distribution of the number of normal (Mean±Std error of mean:23.47± 0.7129) (Std Dev:13.11±0.0541) and ovarian cancer (Mean±Std error of mean:51.62±1.153) (Std Dev:22.86±0.8153) nuclei based on Area values acquired from lamin A stained tissue images before pre-processing.
- B. 2. Comparative distribution of the number of normal (Mean±Std error of mean:19.94± 0.316) (Std Dev:8.414±0.2234) and diseased (Mean±Std error of mean:49.31± 1.234) (Std Dev:26.35±0.8725) nuclei

based on Area values acquired from lamin B stained tissue images before pre-processing.

B. 3. Comparative distribution of the number of normal (Mean±Std error of mean:14.66± 0.3791) (Std Dev:6.577±0.268) and ovarian cancer (Mean±Std error of mean:41.38±1.021) (Std Dev:19.24±0.722) nuclei based on Area values acquired from lamin A stained tissue images after pre-processing.

B. 4. Comparative distribution of the number of normal (Mean±Std error of mean:13.02± 0.3677) (Std Dev:6.401±0.26) and ovarian cancer (Mean±Std error of mean:42.44±1.006) (Std Dev:18.13±0.7111) nuclei based on Area values acquired from lamin B stained tissue images after pre-processing.

Training a Deep Hybrid Learner

After the pre-processed images were acquired, we had to split the data into a training set and validation set with a split ratio of 75:25. The training set was used to train the supervised binary classification model and the validation set was used for hyper-parameter tuning to make sure that the model was not over-fitting on the training set and remained generalized. For training a Deep Hybrid Learner, we first trained the 21 Layered CNN which is used to extract features. We trained it for 250 epochs and the model learning and loss curves obtained are shown in Figure 6. The training and validation learning and loss curve clearly showed that the model was neither over-fitting, nor under-fitting and thus it showed a very good fit. In the model learning curve, we used AUC Score as the metric for determining the fitness of the algorithm. We observed from the learning curve that the training and validation AUC Scores gradually increased with training iterations or epochs and the maximum training score after 250 epochs was obtained as 0.998 and the validation score was obtained as 0.997. The model loss curves for the training and validation set showed that the training and validation loss was gradually decreasing with increase in epoch, which was an indication that the model was learning gradually with more training iteration. Absence of any statistically significant variance between training and validation loss indicated absence of any over-fitting issues. These scores and extremely minimal model loss values along with graphical interpretations from the learning and loss curve supported the fact that the model was quite well generalized and expected to perform well on the test dataset.

Selection of Model Evaluation Matrices

Since, we had a highly imbalanced dataset; accuracy alone would never be a good metric and could be misleading. If the model was always predicting the output as the majority class label, then the accuracy values would be very high, but yet the model would be highly biased on the majority class. Hence, we needed a metric that could show us the impact of true positives and false positives on an imbalanced dataset. Hence, we used Area under the Receiver Operating Characteristics Curve (AUC-ROC) scores (Figure 6) and Confusion matrix to clearly highlight the true positives, true negatives, false positives and false negatives, with the positive class being detection of cancer cells and the negative class being detection of normal cells. In our case, since AI driven approaches were used as automated pre-checks for cancer detection, after which detailed tests and inspection would be performed, false positives were comparatively less expensive than false negatives, as false negatives would lead to delayed detection of

cancer. Typically then, a model with a specific set of hyper-parameters giving maximum AUC-ROC score, minimum false positives, and false negatives needs to be selected, in which less proportion of false negatives as compared to false positives will be preferred. .

Model Evaluation on Test Data:

The clinical details of the TMA samples were revealed and it contained a mixed cohort of tissues from Non cancer ovary as well as from omentum and adjacent areas from patients diagnosed with ovarian cancer undergoing debulking surgery. The normal and cancer tissue samples were grouped in 7 sub-classes (PDS adjacent Normal, PDS Tumor, IDS good response adjacent Normal, IDS good response Tumor, IDS poor response Normal, IDS poor response Tumor, Non cancer ovary)(Figure 7). One representative image from each sub-class was chosen as test image to evaluate the model performances. We compared performances of deep hybrid learning models (Deep Hybrid Learning with Random Forest³⁵ and Deep Hybrid Learning with XGBoost³⁶) with other models like conventional deep neural network (DNN) model, Densenet 201³¹ with transfer learning model³⁷, ResNet50 with transfer learning model³⁷, InceptionNetv3 with transfer learning model³⁷, VGG 16³² with transfer learning model³⁷. The main difference between DHL and conventional DNN is that conventional DNN uses a fully connected neural network, whereas DHL uses a classical Machine Learning algorithm for final classification. In the transfer learning models, we have used pretrained weights from ImageNet. The training, validation and test dataset was same for all the approaches and the number of epochs, batch size was also consistent for all the approaches. Confusion matrices were obtained for the 7 representative images from 7 sub-classes. The Deep Hybrid Learners exhibited 100% validation accuracy by recognising 4 images from 4 sub-classes (PDS adjacent Normal, IDS good response adjacent Normal, IDS poor response Normal and Non-Cancer Ovary, respectively) as true negatives or Normal and 3 images from 3 sub-classes (PDS Tumor, IDS good response Tumor, IDS poor response Tumor, respectively) as true positive or Cancer, whereas the other models could not recognise all 7 images accurately resulting in lower validation accuracies. 'Normal' and 'Cancer' has been annotated as 0 and 1 respectively in the confusion matrices. These images were absolutely unknown to the model and the clinical details were not revealed to the person performing the tests to ensure an unbiased validation and impartial selection of the accurate model based on performance. The matrices were used as the score cards to evaluate the model performances. So, deep hybrid learners were found to be the best working models for this specific problem (Figure 8). For this research work, the choice of the ideal model architecture depends on two main criteria: Generalization and Efficiency. A model is said to be generalized when it is not over-fitting on training data and the model evaluation scores are consistent for training set, validation set and testing set. From the above results we can see that the Deep Hybrid Learners (both Random Forest and XGBoost variant) showed almost consistent results for training, validation and testing phases. Also, we found that the model was extremely efficient with low variance, as we observed that the AUC scores on training validation and test dataset were 0.99, 0.99 and 1.0 respectively (Table 1). The conventional deep learning model trained from scratch without transfer learning, seemed to have high training scores, but it showed high variance on validation and test dataset as the scores were much lower on validation and test set.

Therefore, it indicated that the model was over fitting on the training data, and it was not generalized, hence performing poorly on testing and validation dataset. This behaviour of the model could be explained by our previous hypothesis that the dataset used for this research work was not favourable for a conventional deep learning approach, as it would require more training samples for the conventional model to learn and improve generalization. Hence, more sophisticated and novel approaches like Deep Hybrid Learning which uses CNN for feature extraction and classical machine learning algorithms for the final classification, was more efficient and robust for this type of microscopic image datasets. We have even applied Transfer Learning³⁷ with more sophisticated Deep Learning architectures like DenseNet201³¹, ResNet50, InceptionNetv3, VGG16³², but the results obtained showed presence of over-fitting, lack of generalization and much lower model efficiency than the Deep Hybrid Learners. One plausible reason could be that these transfer learning models were trained using pre-trained weights from ImageNet images, which were significantly different and might have a significant statistical difference from microscopic images, making transfer learning approach ineffective in this case.

Thus we can conclude that our Deep Hybrid learning approach was successful and much better performing than other deep learning algorithms with these types of microscopic image datasets for automated detection of ovarian cancer.

Deep Hybrid Learning

The trained and hyper-parameter tuned model performance on the test set proved how well the model was generalized and did not have any unwanted bias. Now, as imbalanced dataset is not suitable for classical deep learning models for building supervised classifiers with high accuracy and generalization, we came up with the Deep Hybrid Learning (DHL) algorithm, which utilized Deep Convolutional Neural Network to extract features from the pre-processed samples and uses the extracted feature vector with classical Machine Learning algorithms like Random Forest³⁵ and XGBoost³⁶ to build the final classifier. Of late Ensemble learning techniques like Boosting algorithms are known to work well with high dimensional data, as boosting techniques are known to combine weak learners to identify the “hard” data points and combine the weak learners to form a very strong and efficient classifier³⁸. Similarly, Ensemble methods like Random Forests work very well on smaller but high dimensional datasets for solving binary classification problems and have been known to produce generalized results³⁵. The results obtained using the Deep Hybrid Learning approaches turned out to be extremely promising (Figure 8, Table 1) and so far have performed much better than any other conventional approaches and is comparable to or even better than human level performance for this classification problem.

Table 1: Comparison of model evaluation matrices

Model Architecture	Training AUC Score	Validation AUC Score	Testing AUC Score
Deep Hybrid Learner with Random Forest	0.99	0.99	1.0
Deep Hybrid Learner with XGBoost	0.99	0.99	1.0
Conventional Deep Neural Network (without Transfer Learning)	0.99	0.88	0.88
DenseNet201 with Transfer Learner	0.91	0.70	0.67
ResNet50 with Transfer Learning	0.98	0.52	0.83
InceptionNet v3 with Transfer Learning	0.50	0.50	0.50
VGG16 with Transfer Learning	0.96	0.81	0.58

Conclusion

We have introduced nuclear lamins (lamin A and lamin B), which are residents of nuclear boundary and are 'guardians' of the nuclei controlling nuclear morphology. Hence their altered expression or distribution acts as a function of nuclear shape and size and has been used as the tool to detect and diagnose malignancy in context of ovarian cancer. Confocal images of tissue samples elucidated a significant increase in area and perimeter in the ovarian cancer nuclei which is in well agreement to the fact that the cell nuclei in the ovarian tumor tissues are mostly associated with an enlargement in size compared to the cell nuclei of normal tissues. Progressively, we increased the sample size and attempted to evaluate the possibility of quantitative feature extraction of nuclei and characterisation by projecting nuclear morphology as a potential tool to distinguish normal and ovarian cancer tissues by introducing a novel deep hybrid learning network. We first focussed on extracting the pattern of the images and then moving a step further, noise reduction was performed so that it becomes convenient for the model to distinguish between cancer and normal tissue images. Pre-processing the images using various advanced mathematical and morphological techniques, like sharpening, masking, smoothing etc. enhanced the differentiating pattern of the images so that the neural model could easily identify them with utmost precision. This was followed by advanced techniques of data augmentation to create all sort of simulated practical tests by training the deep neural network model over the microscopic image dataset, using the Deep Hybrid learning approach, resulting in a much more reliable system than standard CNN.

Findings and Significance:

But, it's a challenging problem to custom tailor the process of feature extraction in order to classify cancer from microscopic image dataset with fastness and precision. On the other hand, modern techniques of deep learning have already proven its superiority to perform image classification with minimal pre-processing and in many cases it has outperformed domain experts in classifying images. Thus, we decided to use Deep Learning approaches based on CNN (Convolutional neural network) for our study. A typical CNN involves one input and one output layer along with one or multiple hidden layers where convolution occurs through multiplication or other dot products and they are all connected with several nonlinear activation functions. For this specific problem, we believe that the distribution of lamins and size of the nucleus are important factors to classify images with cancer and normal nuclei. Thus, we have trained a deep learning network specifically crafted *denovo* for the particular challenge of classifying ovarian cancer. Different types of augmentation bring almost all possible kinds of representation of the images resulting in a much higher possibility that a real time test image would be very similar if not exactly same and would be having greater probability to be classified with perfection in real time. Also, the drop out used here was 0.20 which is a regularization technique used for preventing over fitting of models. We have introduced a combination of classical machine learning algorithms (XGBoost, SVM, Random Forest) with standard CNN and designed a state of the art deep hybrid network. We created a completely automated pipeline architecture starting from processing images to predicting a cancer or a non-cancer which would be performed within seconds. The strength of our method lies in the fact that the model showed 99.8% training accuracy and 99.7% validation accuracy in distinguishing normal and ovarian cancer cell nuclei and with our feedback mechanism the network could be retrained with wrong predictions made to further improve the accuracy. So a more robust model could be made which outperformed clinical precision in terms of speed and accuracy. As the problem is as unique as ovarian cancer detection using patterns of images, we did not rely over the pre-trained CNN models rather we focused to train a deep learning model tailor-made for solving this particular problem and made it much more operational in real life circumstances rather restricting it to be an academic research tool. As part of our experiment, we used transfer learning models like ResNet50, AlexNet, VGG-16, DenseNet and our custom model had outperformed all of them. That is why it was obvious that the transformation and feature engineering was the main differentiator for solving this particular problem. From the set of experiments conducted, we can clearly observe that our approach works really well for small and imbalanced nuclear morphology image dataset. And the metric scores obtained are much better than other state of the art Deep Learning architectures like DenseNet201 and even when the approach of transfer learning failed. One of the main reasons for Deep Hybrid Learning to be successful is because we had replaced the final fully connected layers with a machine learning (typically ensemble learning) algorithm, which made the overall model efficient and generalized.

Limitations:

Nonetheless, we were restricted to a limited test dataset. Also, for the initial feature extraction, we had used a custom CNN. But based on the results obtained on the conducted experiments, we can conclude that our framework is robust and efficient and worked perfectly well. So, it is certain that with sufficient images in future this would outperform other models and will be able to classify not only between normal

and cancer nuclei but will also be able to predict the degree of risks of benign nuclei to become cancerous.

Current status:

The strength and future research direction for using AI for cancer prediction and early diagnosis should be concerted on cancers which currently do not have a clear natural history identified and therefore a screening strategy. Most female genital tract malignancies possess identifiable precursors except for ovarian malignancies which is the 8th leading cause of cancer mortality among women and 7th leading cause of cancer diagnosis worldwide and 3rd most common women's cancer in India³⁹. GLOBOCAN predicts a 56% increase in ovarian cancer incidence worldwide by 2050- and majority (75%) of cancers are still diagnosed in late stages⁴⁰. We plan to extend our work in larger datasets and especially in diverse chemotherapy response categories; especially supplementing chemotherapy response score (CRS) after neoadjuvant chemotherapy and interval debulking surgery, where CRS2 score is the grey zone and requires better biomarkers for prognostic stratification. We predict a large scope for our approach of interpreting alterations in cellular architecture in the early detection and screening strategies in ovarian cancer. Majority of HGS (High grade serous) ovarian cancers arise from fallopian tubes; many women undergo fimbriectomy for sterilisation purposes as well as a prophylactic measure for prevention of ovarian cancer in high-risk individuals i.e., BRCA mutations. It would be interesting to study whether alteration in the nuclear architecture in fimbria/ovary could be one of the early predictors for developing cancer. More importantly, this may be used as prognostic marker in addition to the standard immunohistochemistry and histology in ovarian cancer if a clinical correlation can be shown in future studies and that remains one of our target research strategies in the future including application in other women cancers. A lot of studies are trying to detect precursor lesion signatures like STIC (serous tubal intraepithelial cancer) and p53 signature in ovarian/tubal cancer; NUMODRIL approach can add to these models for improving diagnostic accuracy.

Future Scope:

As a future scope we would try to test the framework on a larger test dataset and replace the custom CNN with custom transformer architecture to obtain more contextual information from the data and evaluate if the custom transformer architecture version is giving better result. The novelty of this work lies in the fact that this pipeline christened as NUMODRIL could be generalized as a global technique in the diagnosis and prognosis of all types of neoplasia which might be associated with changes in nuclear architecture as a result of alteration of lamin A/B expression profile.

Declarations

Acknowledgements:

All tissues and TMA samples were obtained from Tata Medical Center , provided by AsimaMukhopadhyay , a clinician scientist (Gynaecological Oncologist), based at Tata Medical Center

and currently at Chittaranjan National Cancer Institute Kolkata and her research group. Biobanking for ovarian cancer tissues and TMA creation was performed through the DST-UKIERI grant held by Dr. Asima Mukhopadhyay. The histograms were generated using ROOT data analysis framework with the help of Mr. Gourab Saha, SRF, High Energy Nuclear and Particle Physics Division, SINP who helped in writing the programs in C++. Duhita Sengupta thanks DAE for the fellowship. Kaushik Sengupta thanks SERB, DST & BARD project of DAE, Govt. of India.

Authors' Contribution:

Duhita Sengupta: Methodology, Validation, Formal Analysis, Investigation, Data Curation, Writing-Original Draft, Writing-Review and Editing, Visualization. **SkNishan Ali.:** Methodology, Software, Validation, Investigation, Data Curation, Writing-Original Draft, Writing-Review and Editing, Visualization. **Aditya Bhattacharya:** Methodology, Software, Validation, Investigation, Data Curation, Writing-Original Draft, Writing-Review and Editing, Visualization. **Joy Mustafi :** Methodology, Software, Validation, Investigation, Data Curation, Writing-Original Draft, Writing-Review and Editing, Visualization. **Asima Mukhopadhyay.:** Methodology, Validation, Clinical Investigation, Data Curation Writing-Review and Editing. **Kaushik Sengupta:** Conceptualization, Methodology, Validation, Data Curation, Resources, Writing-Original Draft, Writing-Review and Editing, Visualization, Supervision, Project Administration, Funding Acquisition.

Competing interest: No

References

1. Bhattacharjee, P., Banerjee, A., Banerjee, A., Dasgupta, D. & Sengupta, K. Structural alterations of Lamin A protein in dilated cardiomyopathy. *Biochemistry* **52**, 4229-4241, doi:10.1021/bi400337t (2013).
2. Zuela, N., Bar, D. Z. & Gruenbaum, Y. Lamins in development, tissue maintenance and stress. *EMBO Rep* **13**, 1070-1078, doi:10.1038/embor.2012.167 (2012).
3. Briand, N. & Collas, P. Laminopathy-causing lamin A mutations reconfigure lamina-associated domains and local spatial chromatin conformation. *Nucleus* **9**, 216-226, doi:10.1080/19491034.2018.1449498 (2018).
4. Naetar, N., Ferraioli, S. & Foisner, R. Lamins in the nuclear interior - life outside the lamina. *J Cell Sci* **130**, 2087-2096, doi:10.1242/jcs.203430 (2017).
5. Pfeifer, C. R., Vashisth, M., Xia, Y. & Discher, D. E. Nuclear failure, DNA damage, and cell cycle disruption after migration through small pores: a brief review. *Essays Biochem* **63**, 569-577, doi:10.1042/EBC20190007 (2019).
6. Marmiroli, S. *et al.* A-type lamins and signaling: the PI 3-kinase/Akt pathway moves forward. *J Cell Physiol* **220**, 553-561, doi:10.1002/jcp.21807 (2009).

7. Kreienkamp, R. & Gonzalo, S. Hutchinson-Gilford Progeria Syndrome: Challenges at Bench and Bedside. *Subcell Biochem* **91**, 435-451, doi:10.1007/978-981-13-3681-2_15 (2019).
8. Prokocimer, M., Barkan, R. & Gruenbaum, Y. Hutchinson-Gilford progeria syndrome through the lens of transcription. *Aging Cell* **12**, 533-543, doi:10.1111/accel.12070 (2013).
9. Bartoletti-Stella, A. *et al.* Messenger RNA processing is altered in autosomal dominant leukodystrophy. *Hum Mol Genet* **24**, 2746-2756, doi:10.1093/hmg/ddv034 (2015).
10. Elkhatab, R. *et al.* Nuclear envelope remodelling during human spermiogenesis involves somatic B-type lamins and a spermatid-specific B3 lamin isoform. *Mol Hum Reprod* **21**, 225-236, doi:10.1093/molehr/gau111 (2015).
11. Shimi, T. *et al.* Structural organization of nuclear lamins A, C, B1, and B2 revealed by superresolution microscopy. *Mol Biol Cell* **26**, 4075-4086, doi:10.1091/mbc.E15-07-0461 (2015).
12. Dittmer, T. A. & Misteli, T. The lamin protein family. *Genome Biol* **12**, 222, doi:10.1186/gb-2011-12-5-222 (2011).
13. Xiong, Z. M., LaDana, C., Wu, D. & Cao, K. An inhibitory role of progerin in the gene induction network of adipocyte differentiation from iPS cells. *Aging (Albany NY)* **5**, 288-303, doi:10.18632/aging.100550 (2013).
14. Piekarowicz, K. *et al.* The effect of the lamin A and its mutants on nuclear structure, cell proliferation, protein stability, and mobility in embryonic cells. *Chromosoma* **126**, 501-517, doi:10.1007/s00412-016-0610-9 (2017).
15. Sengupta, D., Mukhopadhyay, A. & Sengupta, K. Emerging roles of lamins and DNA damage repair mechanisms in ovarian cancer. *Biochem Soc Trans* **48**, 2317-2333, doi:10.1042/BST20200713 (2020).
16. Cantwell, H. & Nurse, P. Unravelling nuclear size control. *Curr Genet* **65**, 1281-1285, doi:10.1007/s00294-019-00999-3 (2019).
17. Richter, K., Nessling, M. & Lichter, P. Macromolecular crowding and its potential impact on nuclear function. *Biochim Biophys Acta* **1783**, 2100-2107, doi:10.1016/j.bbamcr.2008.07.017 (2008).
18. Bera, M. & Sengupta, K. Nuclear filaments: role in chromosomal positioning and gene expression. *Nucleus* **11**, 99-110, doi:10.1080/19491034.2020.1769445 (2020).
19. Irianto, J., Pfeifer, C. R., Ivanovska, I. L., Swift, J. & Discher, D. E. Nuclear lamins in cancer. *Cell Mol Bioeng* **9**, 258-267, doi:10.1007/s12195-016-0437-8 (2016).
20. Radhakrishnan, A., Damodaran, K., Soylemezoglu, A. C., Uhler, C. & Shivashankar, G. V. Machine Learning for Nuclear Mechano-Morphometric Biomarkers in Cancer Diagnosis. *Sci Rep* **7**, 17946, doi:10.1038/s41598-017-17858-1 (2017).
21. Tamunomie, N. 129-143 (2015).
22. BenTaieb, A., Li-Chang, H., Huntsman, D. & Hamarneh, G. A structured latent model for ovarian carcinoma subtyping from histopathology slides. *Medical Image Analysis* **39**, 194-205, doi:https://doi.org/10.1016/j.media.2017.04.008 (2017).

23. Mueller, J. L. *et al.* Rapid staining and imaging of subnuclear features to differentiate between malignant and benign breast tissues at a point-of-care setting. *J Cancer Res Clin Oncol* **142**, 1475-1486, doi:10.1007/s00432-016-2165-9 (2016).
24. Rubin, M. *et al.* TOP-GAN: Stain-free cancer cell classification using deep learning with a small training set. *Medical Image Analysis* **57**, 176-185, doi:https://doi.org/10.1016/j.media.2019.06.014 (2019).
25. Huttunen, M. J. *et al.* Automated classification of multiphoton microscopy images of ovarian tissue using deep learning. *J Biomed Opt* **23**, 1-7, doi:10.1117/1.JBO.23.6.066002 (2018).
26. Wang, Z. Y. *et al.* Bladder Cancer-Specific Nuclear Matrix Proteins-4 May Be a Potential Biomarker for Non-Muscle-Invasive Bladder Cancer Detection. *Dis Markers* **2018**, 5609395, doi:10.1155/2018/5609395 (2018).
27. Chen, X. *et al.* Overexpression of nuclear AR-V7 protein in primary prostate cancer is an independent negative prognostic marker in men with high-risk disease receiving adjuvant therapy. *Urol Oncol* **36**, 161 e119-161 e130, doi:10.1016/j.urolonc.2017.11.001 (2018).
28. Dey, P. Cancer nucleus: morphology and beyond. *Diagn Cytopathol* **38**, 382-390, doi:10.1002/dc.21234 (2010).
29. Xia, Y. *et al.* Nuclear rupture at sites of high curvature compromises retention of DNA repair factors. *J Cell Biol* **217**, 3796-3808, doi:10.1083/jcb.2017111161 (2018).
30. Fernández, A., García, S., Herrera, F. & Chawla, N. V. SMOTE for learning from imbalanced data: progress and challenges, marking the 15-year anniversary. *J. Artif. Int. Res.* **61**, 863–905 (2018).
31. Yu, X., Zeng, N., Liu, S. & Zhang, Y.-D. Utilization of DenseNet201 for diagnosis of breast abnormality. *Machine Vision and Applications* **30**, 1135-1144, doi:10.1007/s00138-019-01042-8 (2019).
32. Simonyan, K. & Zisserman, A. Very Deep Convolutional Networks for Large-Scale Image Recognition. *CoRR* **abs/1409.1556** (2015).
33. Blagus, R. & Lusa, L. SMOTE for high-dimensional class-imbalanced data. *BMC Bioinformatics* **14**, 106, doi:10.1186/1471-2105-14-106 (2013).
34. Nandini, D. B. & Subramanyam, R. V. Nuclear features in oral squamous cell carcinoma: A computer-assisted microscopic study. *J Oral Maxillofac Pathol* **15**, 177-181, doi:10.4103/0973-029X.84488 (2011).
35. Fawagreh, K., Gaber, M. M. & Elyan, E. Random forests: from early developments to recent advancements. *Systems Science & Control Engineering* **2**, 602-609, doi:10.1080/21642583.2014.956265 (2014).
36. Chen, T. & Guestrin, C. *XGBoost: A Scalable Tree Boosting System.* (2016).
37. Weiss, K., Khoshgoftaar, T. M. & Wang, D. A survey of transfer learning. *Journal of Big Data* **3**, 9, doi:10.1186/s40537-016-0043-6 (2016).
38. Mayr, A., Binder, H., Gefeller, O. & Schmid, M. The evolution of boosting algorithms. From machine learning to statistical modelling. *Methods Inf Med* **53**, 419-427, doi:10.3414/ME13-01-0122 (2014).

39. Coburn, S. B., Bray, F., Sherman, M. E. & Trabert, B. International patterns and trends in ovarian cancer incidence, overall and by histologic subtype. *Int J Cancer* **140**, 2451-2460, doi:10.1002/ijc.30676 (2017).
40. Bray, F. *et al.* Global cancer statistics 2018: GLOBOCAN estimates of incidence and mortality worldwide for 36 cancers in 185 countries. *CA Cancer J Clin* **68**, 394-424, doi:10.3322/caac.21492 (2018).

Figures

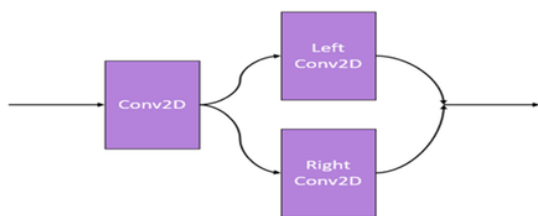
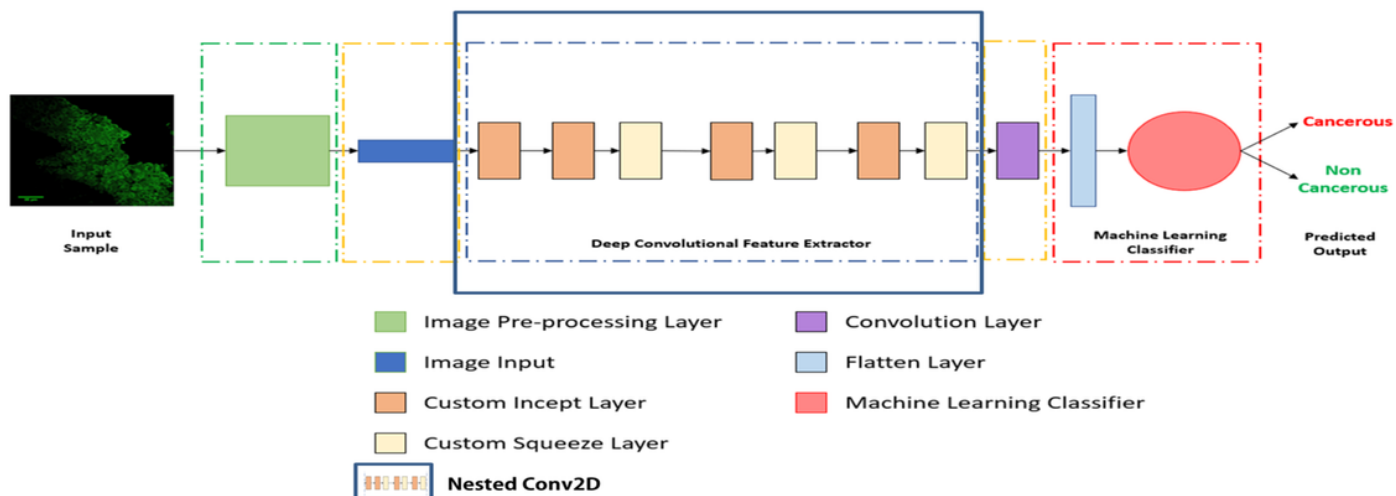


Figure 1

The overall scheme of deep hybrid learning algorithm.

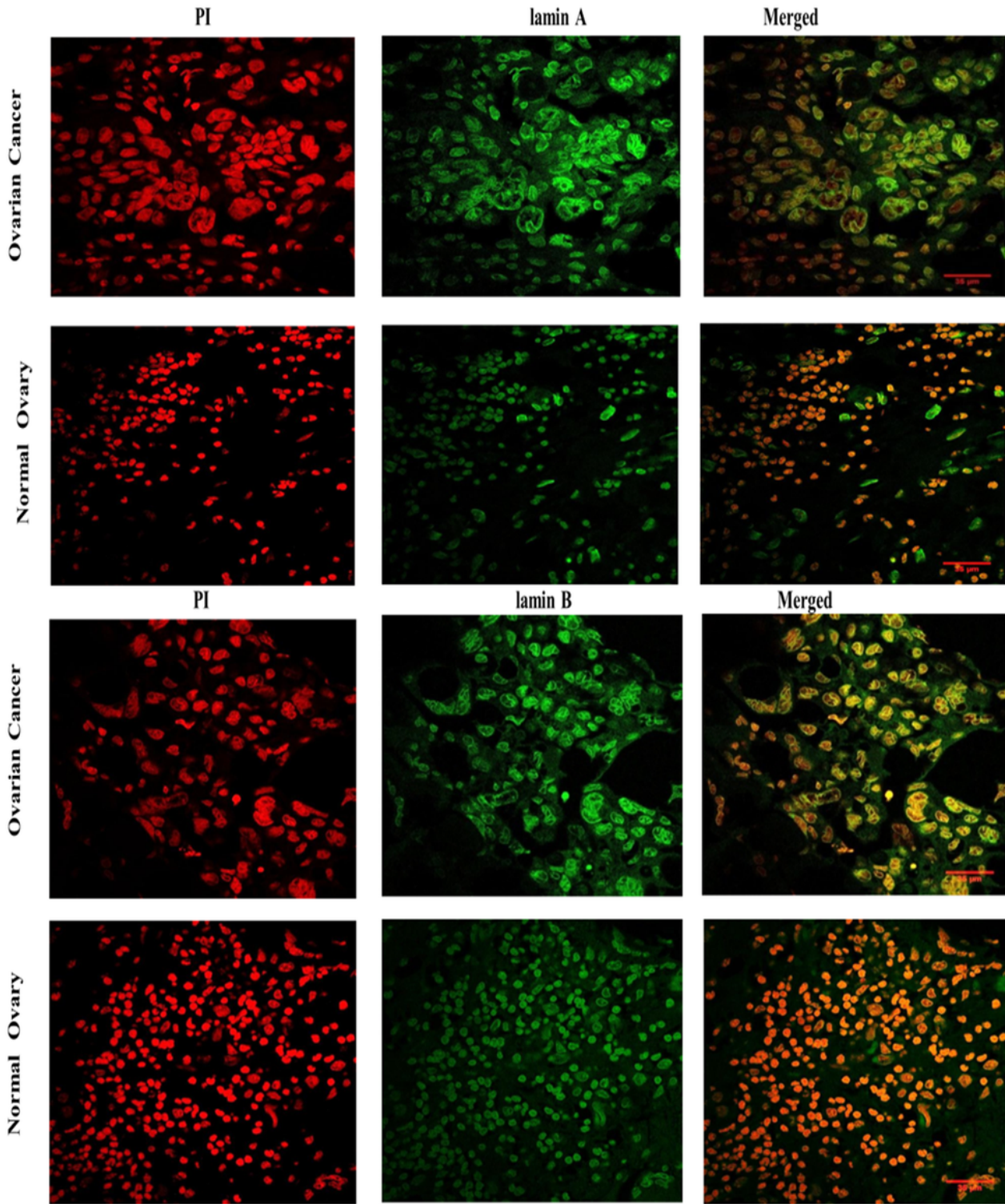


Figure 2

Representative Fields of confocal micrographs showing distribution of lamin A and lamin B in tissues from Ovarian cancer and Normal Ovary. Images of Ovarian Cancer and Normal ovarian tissue nuclei have been marked in their respective columns. Propidium Iodide staining of the nuclei is shown in the first panel containing red channel images. Lamin A and lamin B distributions respectively have been shown in

the second panel of green channel images. Merged images of both the channels have been shown in the third panel. Magnification: 63X. Scale Bar: 35 μ m

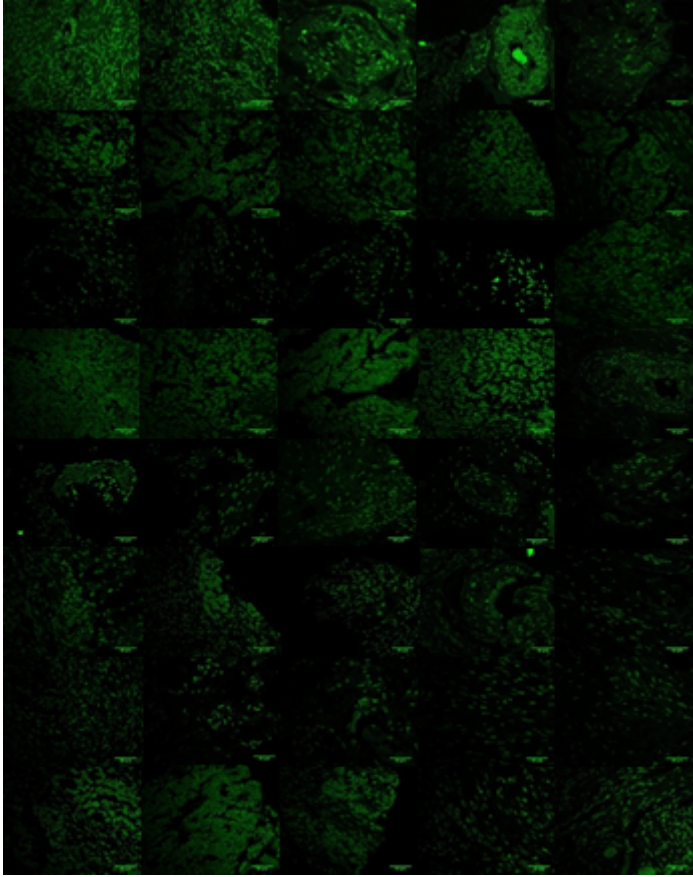


Figure 3

40 samples in a tissue microarray slide stained with lamin A. Each field has been captured under Magnification: 63x. Scale Bar: 35 μ m

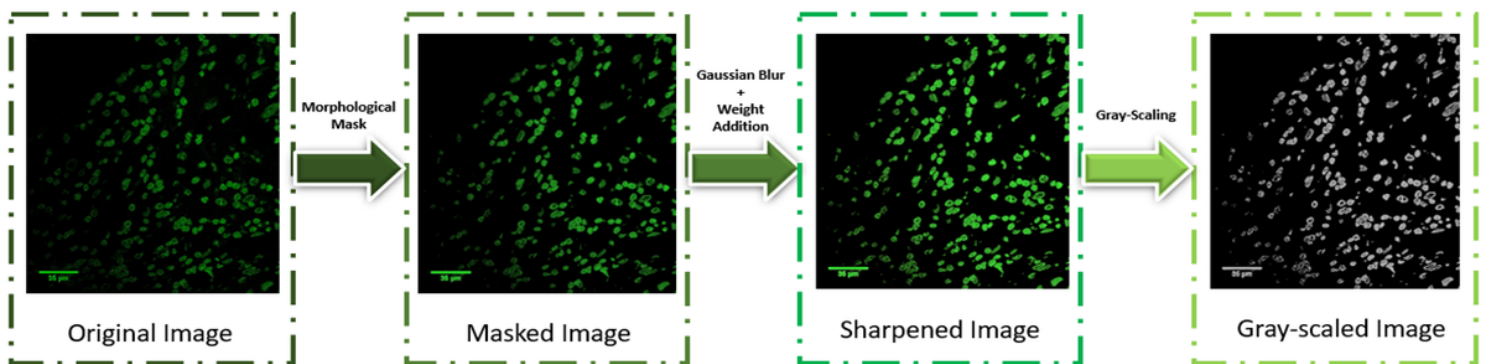


Figure 4

Sequence of operations followed for pre-processing of the image dataset: In the first part, segmentation mask was applied based on the morphometric properties followed by image sharpening to have the key features more visually prominent. In the second part, the sharpened image, which was obtained using

Gaussian Blurring and weight addition, was transformed to its gray scale version to improve the computational time of the model.

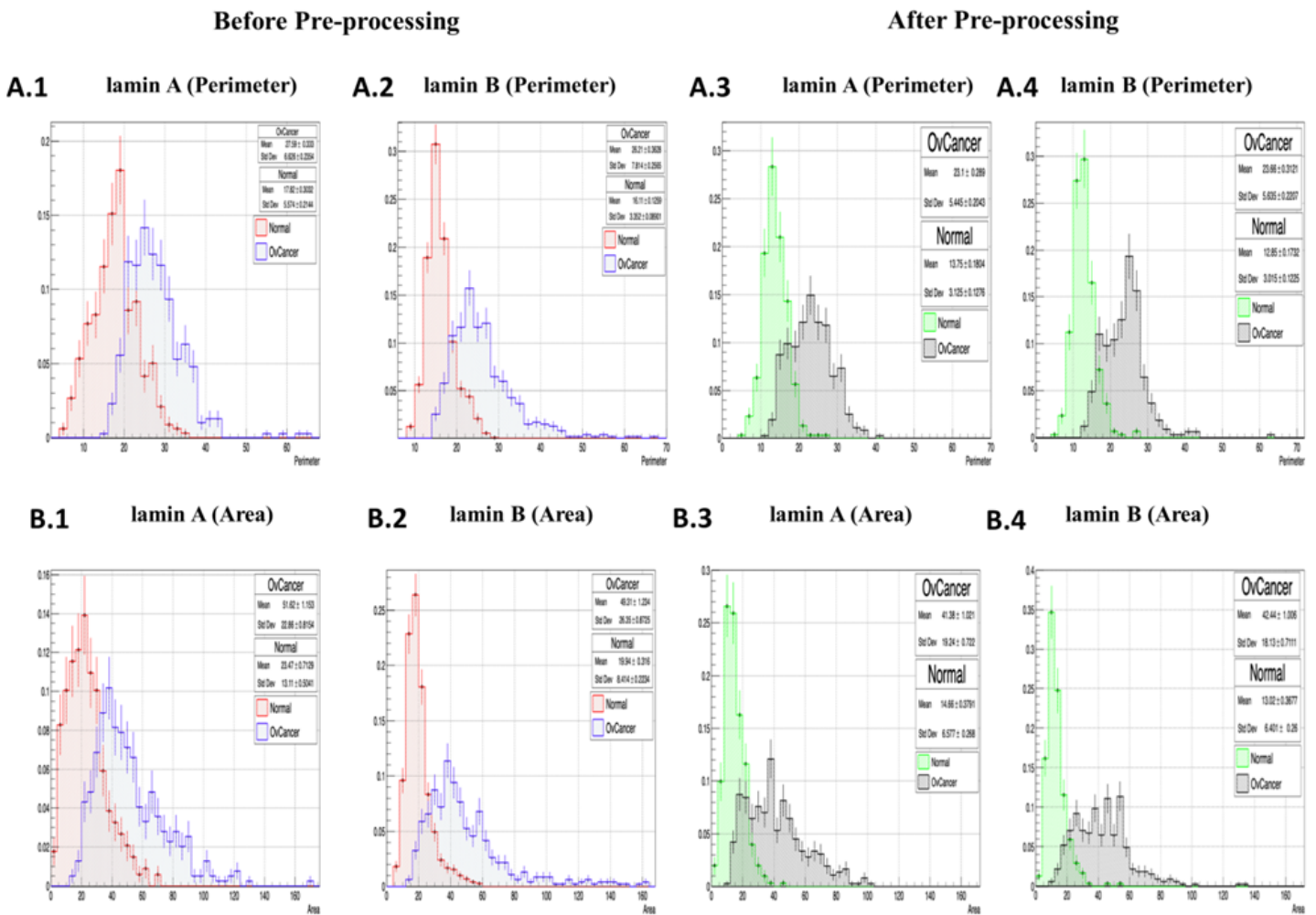


Figure 5

Histograms showing distributions of the normal and Ovarian Cancer nuclei based on different morphometric parameters obtained from lamin A and B stained tissue sample images before and after pre-processing. X axis denotes the normalised number of nuclei with respect to the total number of nuclei calculated. Y axis denotes the measure of the parameter.

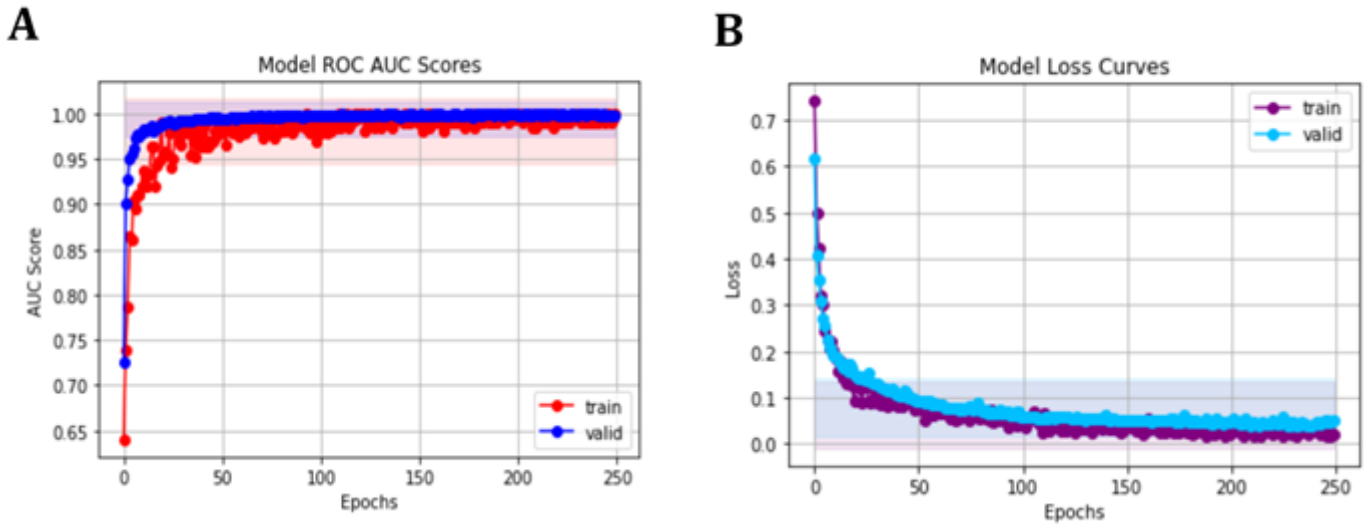


Figure 6

The plots detailing the pattern of A. Model learning curve based on the information obtained from 250 epochs. Training AUC score has been depicted in red and validation AUC score has been depicted in blue. Both training and validation AUC scores have increased in every epoch. 0.998 and 0.997 are the maximum training and validation scores respectively after 250 epochs. B. Model loss curve based on the information obtained from 250 epochs. Training loss has been depicted in violet and validation loss has been depicted in blue. Training and validation losses are gradually decreasing in every epoch showing absence of any significant over-fitting.

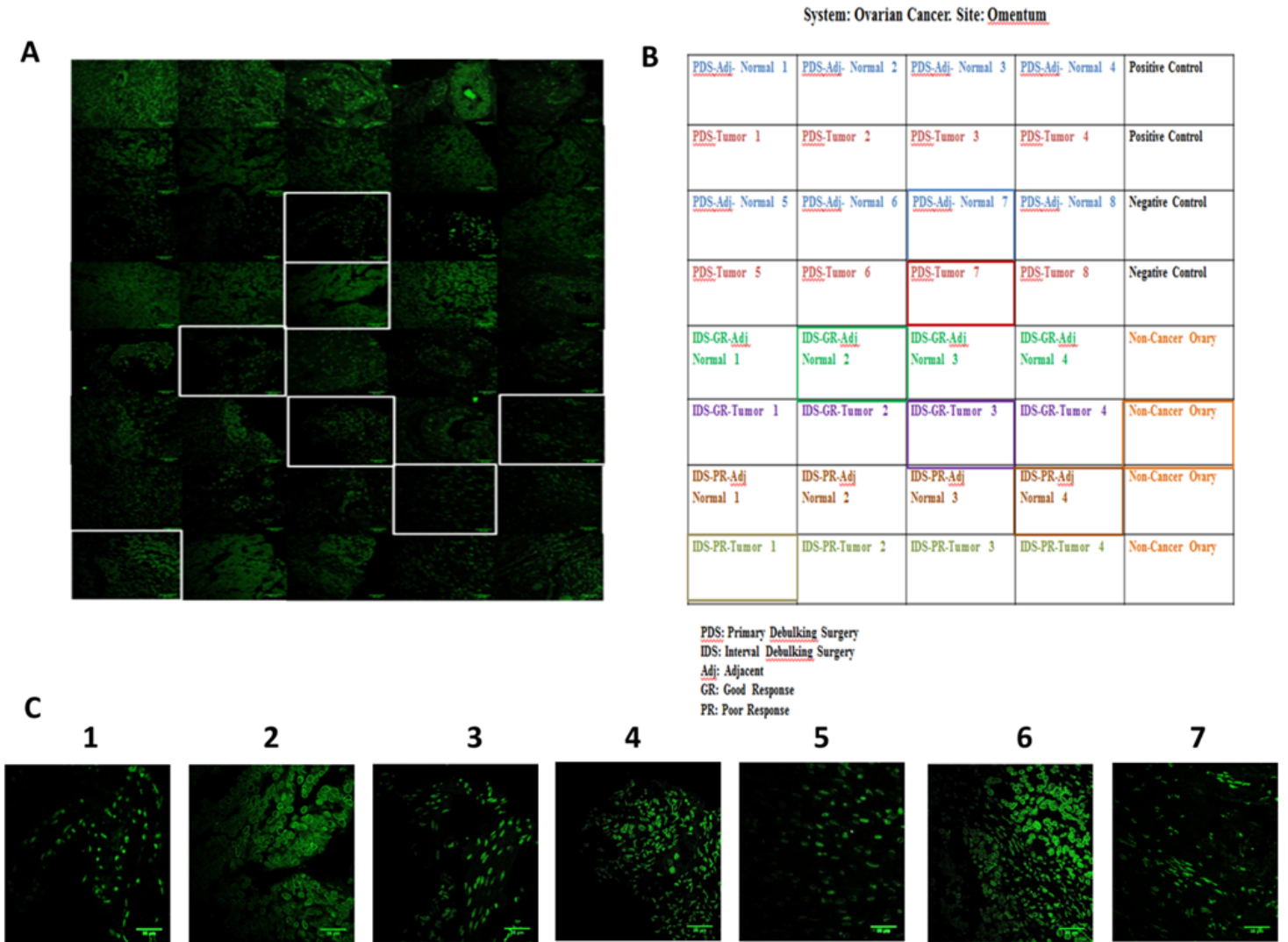


Figure 7

40 tissue samples from the TMA containing a mixed cohort of normal and cancer tissues were grouped in 7 sub-classes and one representative image from each sub-class was used as test image for validation of model performances. A. 40 samples in a tissue microarray slide stained with lamin A. Representative images from 7 sub-classes have been marked in white boxes. Each field has been captured under Magnification: 63x. Scale Bar: 35 μ m. B. Clinical details of microarray sample tissues from Non cancer ovary as well as from omentum and adjacent areas from patients diagnosed with ovarian cancer undergoing debulking surgery. 7 sub-classes have been marked in 7 different colours. Positive and Negative controls have been marked in black. C. Seven representative images which were used as test data for validation of the best working model. Normal and cancer tissues were grouped in seven sub-classes namely, 1. PDS-Adj- Normal 2.PDS-Tumor 3.IDS - GR-Adj Normal 4.IDS-GR-Tumor 5.IDS-PR-Adj Normal 6.IDS-PR-Tumor 7. Non-Cancer Ovary

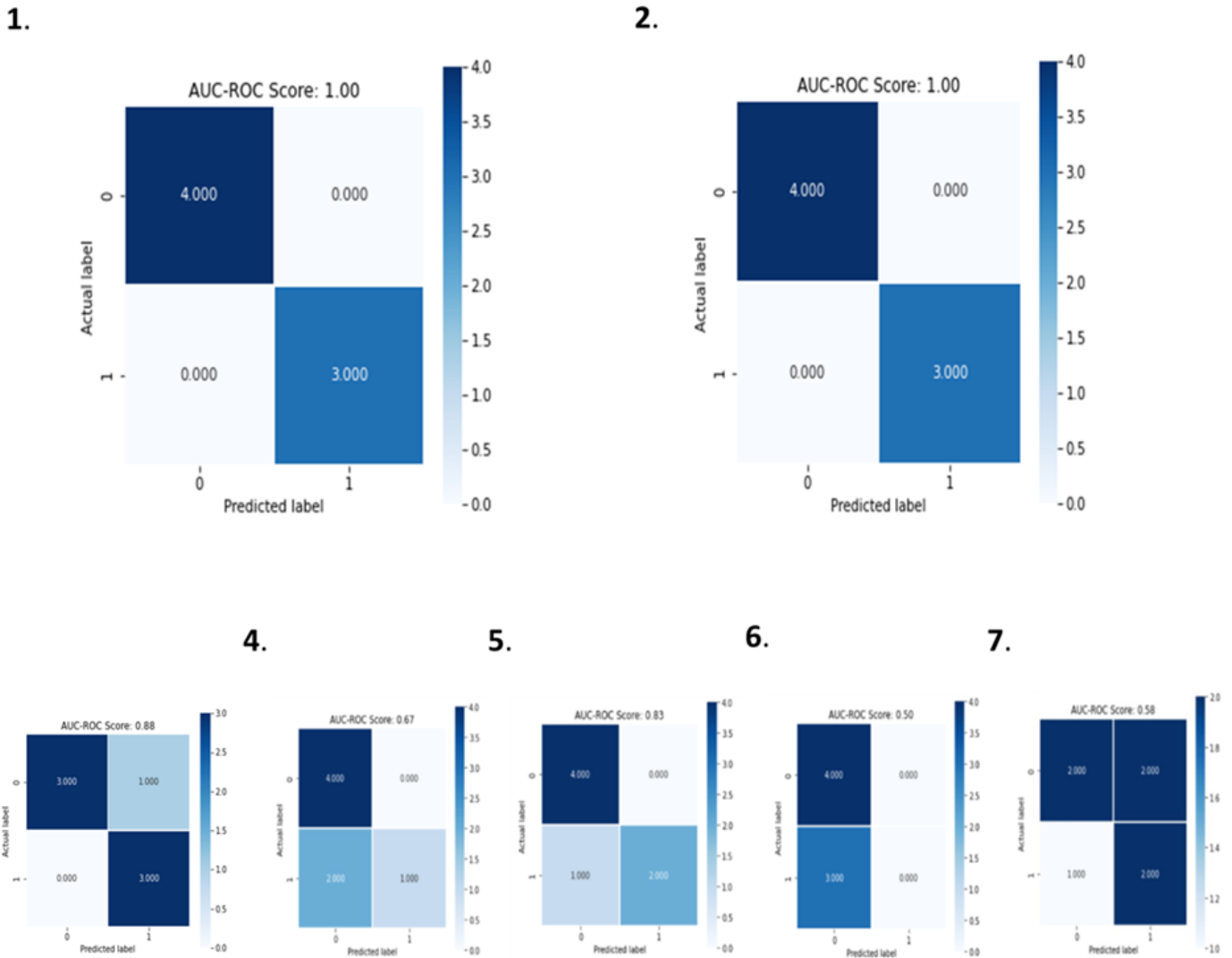


Figure 8

Confusion Matrix on Test Dataset. In this research work we have compared the Deep Hybrid Learning with both XGBoost and Random Forest variant, with a conventional Deep Neural Network (without transfer learning and having the same 21 layered CNN as DHL), DenseNet201 with transfer learning, InceptionNet v3 with transfer learning, ResNet50 with transfer learning and VGG16 with transfer learning. The Deep Hybrid Learners exhibited 100% validation accuracy by accurately identifying 4 images from 4 sub-classes (PDS adjacent Normal, IDS good response adjacent Normal, IDS poor response Normal and Non-Cancer Ovary, respectively) as true negatives or Normal and 3 images from 3 sub-classes (PDS Tumor, IDS good response Tumor, IDS poor response Tumor, respectively) as true positive or Cancer. The other models could not identify all 7 images correctly resulting in lower validation accuracies. 'Normal' and 'Cancer' has been denoted as 0 and 1 respectively in the confusion matrices. 1. Deep Hybrid Learning with Random Forest 2. Deep Hybrid Learning with XGBoost 3. Conventional Deep Neural Network Model 4. DenseNet201 with transfer learning 5. ResNet50 with transfer learning 6. InceptionNetv3 with transfer learning 7. VGG16 with transfer learning

Supplementary Files

This is a list of supplementary files associated with this preprint. Click to download.

- [SupplementaryMaterialScientificReports.docx](#)